Intermetallics 124 (2020) 106844

Contents lists available at ScienceDirect

Intermetallics

journal homepage: www.elsevier.com/locate/intermet

Atomistic calculations of the generalized stacking fault energies in two refractory multi-principal element alloys

Shuozhi Xu [a,*], Emily Hwang [b], Wu-Rong Jian [c], Yanqing Su [c], Irene J. Beyerlein [a,c,d]

[a] California NanoSystems Institute, University of California, Santa Barbara, CA 93106-6105, USA
[b] Department of Chemistry, Harvey Mudd College, Claremont, CA 91711, USA
[c] Department of Mechanical Engineering, University of California, Santa Barbara, CA 93106-5070, USA
[d] Materials Department, University of California, Santa Barbara, CA 93106-5050, USA

ARTICLE INFO

Keywords:
Atomistic simulations
Generalized stacking fault energies
Multi-principal element alloys
Embedded-atom method potential
Density functional theory

ABSTRACT

In this work, we utilize atomistic simulations to calculate the generalized stacking fault energies (GSFEs), which are related to the dislocation glide process, on four types of slip planes – {110}, {112}, {123}, and {134} – in two refractory multi-principal element alloys (MPEAs): MoNbTi and NbTiZr. To serve as a reference material for MoNbTi, we develop, validate, and employ an *A*-atom interatomic potential, which is expected to represent the response of the nominal random solution. Our calculations show that, owing to the variation in local chemical composition within small finite nanometer sized planes, (i) the peak GSFE values vary significantly among parallel planes; (ii) within the same specific {110} plane, substantial differences in the GSFE curves along the two non-parallel ⟨111⟩ directions are observed; (iii) the {110} GSFE curves develop an asymmetry, such that the peak energy is not achieved at half the lattice periodicity length, (iv) the GSFE value after a shift equaling the lattice periodicity length is not recovered; and (v) on average, the peak GSFE values are close to the volume fraction average of the peak GSFEs of their constituents.

1. Introduction

In most traditional multi-element alloy design, there is one principal element that forms the matrix and various additional elements in smaller amounts are added to enhance particular structural properties [1]. In using multi-component phase diagrams, traditional alloy development has been focused on the corners and edges, but not the central region of these diagrams where there are more than one principal elements [2]. In 2004, Yeh et al. [3] and Cantor et al. [4] reported that some carefully chosen equimolar compositions of five elements form stable solid solution phases on an underlying face-centered cubic (FCC) lattice. These alloys are generally termed "multi-principal element alloys (MPEAs)". Studies of FCC MPEAs have discovered many MPEAs of three or more elements to possess outstanding strength and ductility [5]. Later, Senkov et al. [6] developed new equimolar compositions of five elements that formed stable solid solution body-centered cubic (BCC) phases. Reports on the strength and ductility of refractory BCC MPEAs, containing at least one refractory metals (Mo, Nb, Re, Ta, and W), have been equally stunning [7,8], such as retention of high strengths up to 1600 °C [9].

Sharing the same lattice structure as pure BCC metals, the plastic deformation in BCC MPEAs is also governed by the motion of dislocations on particular crystallographic planes [10]. In most crystals, the glide of a dislocation in a crystallographic plane involves in-plane shearing and breaking bonds across the plane [11]. The resistance to dislocation glide is in part related to the potential energy associated with shearing the plane, called the generalized stacking fault energy (GSFE) [12]. GSFEs can be calculated using atomistic techniques such as density functional theory (DFT) or molecular statics (MS) techniques [13]. The calculation entails shearing one half crystal over another half across a specific crystallographic plane.

To date, the GSFE has proven in many ways to play an integral part in understanding or modeling dislocation properties and motion [14]. Key local GSFE minima or maxima, the GSFE variation in one special direction, or even the entire surface considering all in-plane directions are employed to determine the geometry of equilibrium core structures [15,16]. For example, in an FCC pure metal, the local minimum, named the intrinsic stacking fault (ISF) energy, is, to the first order, inversely proportional to the ISF width of an extended dislocation [17,18]. In BCC Fe, the structure and glide stress of an edge dislocation are strongly correlated with the shape of the GSFE curve [19]. Parameterized functions of the GSFE curves or surfaces have been incorporated into phase-field dislocation models [20] to calculate the critical stresses

* Corresponding author.
E-mail address: shuozhixu@ucsb.edu (S. Xu).

https://doi.org/10.1016/j.intermet.2020.106844
Received 15 April 2020; Received in revised form 20 May 2020; Accepted 20 May 2020

required to expand loops from boundaries and surfaces in crystals. GSFE curves have also been used to gain insight into the preferred slip systems in phases that are challenging to test directly, such as pseudo-morphic phases or high-pressure phases [21–23]. GSFE curves containing different amounts of solute atoms on the shear plane have helped to understand the effects of alloy concentrations on slip system propensity [24–26].

The type of atoms, their arrangement, and lattice spacings within and across the plane collectively determine the GSFEs. In pure metals, the GSFE landscape is periodic within the glide plane. However, given the random chemical compositions in MPEAs, it is expected that the GSFE landscapes in them are no longer periodic. As a result, there exists a spatial variation in the GSFE within a sheared plane and among separate parallel planes from the same volume with a nominal distribution. Recent works have demonstrated that the ISF width of initially straight, extended dislocations exhibits an in-plane variation along its length, in many FCC MPEAs, e.g., CoCrNi [27,28], CoFeNi [29], CoCrFeNi [28], CoCuFeNi [29], $Co_{30}Fe_{16.67}Ni_{36.67}Ti_{16.67}$ [30,31], CoCrCuFeNi [32], and CoCrFeMnNi [28]. From any point on the GSFE landscape, shear displacements of a lattice length usually do not recover the same GSFE value, a point demonstrated by CoCrNi MPEAs [27]. As another consequence, unlike in pure metals where all GSFE values are non-negative, some GSFE values in MPEAs may be negative. A number of studies involving atomic scale GSFE calculations of FCC CoNi-based MPEAs, have reported that a substantial fraction of the sampled areas sheared produced negative ISF energy values [27,33,34]. Last, the GSFE values in MPEAs depend on the size of the area being sheared, A_{gsf}, within which the local chemical composition may vary significantly. In a pure metal, a slip plane area size is selected that appropriately represents the lattice structure or in a dilute alloy, its composition. For an MPEA, A_{gsf} would need to be sufficiently large to reflect the composition of the nominal solid solution. Indeed, defining a representative slip plane area in GSFE calculations for a highly concentrated MPEA is not as straightforward. When A_{gsf} is small, the chemical composition within the finite area does not necessarily match that of the 3D volume from which it is taken. Hence, a variation among the GSFE values for different specific glide planes from the 3D volume can be expected. Prior MS calculations in FCC NiFe found that, on the {111} slip planes, a smaller A_{gsf} leads to a larger standard deviation of the ISF energy, while the mean ISF energy value remains unchanged [35].

However, there is value in studying the local variations in the GSFE among different areal regions or crystallographic planes in a volume of MPEA. An individual dislocation does not sample an infinitely large region at any one time. As dislocations sweep across the glide plane in an MPEA, they would encounter regions varying, with atomic scale frequency, in the type of atoms. The potential energy associated with the shear dislocations incur can be expected to constantly change. With respect to the length scales covered by a moving dislocation, it would be useful to understand the potential energies to shear areal regions on the order of one to ten times the Burgers vector.

In this work, using atomistic simulations, we take a first look at the effect of fluctuations in the chemical composition, characteristic of refractory MPEAs, on the variation in the GSFE with shear displacement over one or a few lattice periodicity distances. We study these MPEA effects on GSFEs in two equal-molar ternary refractory alloys, MoNbTi and NbTiZr, which were recently shown to desirably possess low densities and high specific strengths [36–38]. GSFE calculations focus on the four types of slip planes in BCC crystals: {110}, {112}, {123}, and {134}. To quantify the MPEA effect, GSFE calculations are repeated on three pure metals for reference: the two constituent pure BCC metals, Mo and Nb, and a hypothetical pure BCC metal enabled by an *A*-atom interatomic potential, wherein all atoms possess average properties of the MPEA. The interatomic potentials for the MoNbTi and its *A*-atom equivalent are developed and validated here, following those methods employed previously for NbTiZr [39]. We show that the peak GSFE values vary significantly among parallel planes and within the same specific {110} plane, there are substantial differences in the GSFE curves along the two non-parallel ⟨111⟩ directions. Interestingly, we also find that on average, the peak GSFE values are close to the volume fraction average of the peak GSFEs of their constituents.

2. Interatomic potentials

2.1. Alloy and A-atom potentials

Here, embedded-atom method (EAM) potentials are used for each MPEA. The EAM formulation for the potential energy is given by [40]

$$E = \frac{1}{2}\sum_{i}^{N}\sum_{\substack{j\\ j\neq i}}^{N_{\text{nei}}} V(R^{ij}) + \sum_{i} F(\bar{\rho}^{i}) \tag{1}$$

where N is the number of atoms, N_{nei} is the number of neighboring atoms of atom i, V is the pair potential, F is the embedding potential, $\bar{\rho}^{i}$ is the host electron density at atom i, R^{ij} is the norm of vector $\mathbf{R}^{ij}$ pointing from atom i to atom j, i.e.,

$$\mathbf{R}^{ij} = \mathbf{R}^{j} - \mathbf{R}^{i} \tag{2}$$

$$\bar{\rho}^{i} = \sum_{\substack{j\\ j\neq i}}^{N_{\text{nei}}} \rho^{ij}(R^{ij}) \tag{3}$$

where ρ^{ij} is the local electron density contributed by atom j to atom i. Here, formulations of V and ρ^{ij} only involve the type of atom i and the distance between atom i and its neighboring atom j, R^{ij}, regardless of the type of atom j. For example, let atom i be Nb, then V and ρ^{ij} depend only on R^{ij} for any atom j which may be Mo, Ti, or Zr. It follows then that an "alloy potential" can be developed for each MPEA, based on the EAM potential for pure metals, including Mo, Ti, Zr [41], and Nb [42]. This type of potential has been used to account for lattice distortion and chemical disorder in BCC refractory MPEAs, e.g., NbTiZr [39] and NbTaV [43,44], and will be used for the two MPEAs here.

In order to quantify an MPE effect, a reference pure metal needs to be defined and its properties are compared to those of the MPEA. Possible reference metals include two constituent metals, Mo and Nb, which share the same stable BCC crystal structure as the parent MPEA in ambient conditions. Many interatomic potentials currently exist for these two metals, e.g., Refs. [45,46], with varying degrees of suitability for simulating defect energetics and motion. However, for consistency, we elect to employ the same EAM potentials [41,42] used to build the alloy potentials.

As a third material reference, it is possible to consider a hypothetical pure metal, with single atom bond properties consistent with that of the average MPEA. In 2016, the interatomic potential for such a pure metal, named the "average-atom potential" or "*A*-atom potential", was validated in terms of dislocations in MPEAs [47,48]. This type of potential provides a mean-field representation of the MPEA by approximating the interaction between any two elements as a weighted average. As a result, it cannot account for lattice distortion or chemical disorder. *A*-atom potentials have been developed for multiple MPEAs, including, but not limited to, CrFeNi [47], NbTiZr [39], $Co_{16.67}Fe_{36.67}Ni_{16.67}Ti_{30}$ [49], $Co_{30}Fe_{16.67}Ni_{36.67}Ti_{16.67}$ [30], and CoCrCuFeNi [32].

Since there is currently no *A*-atom potential for MoNbTi, this potential is developed here. In what follows, X and Y denote different types of elements. For example, $F^{X}\left(\bar{\rho}_{i}\right)$ is the embedding potential for atom i which is element X. The *A*-atom EAM formulation for the potential energy is [47,48]

$$E = \frac{1}{2}\sum_{i}^{N}\sum_{\substack{j\\ j\neq i}}^{N_{\text{nei}}} V_{ij}^{A}(R^{ij}) + \sum_{i}^{N} F^{A}\left(\langle\bar{\rho}_{i}\rangle\right) \tag{4}$$

where $\langle\cdots\rangle$ takes the average, and

$$F^{A}\left(\langle\bar{\rho}_{i}\rangle\right) = \sum_{X}^{N_{\text{T}}} c^{X} F^{X}\left(\langle\bar{\rho}_{i}\rangle\right) \tag{5}$$

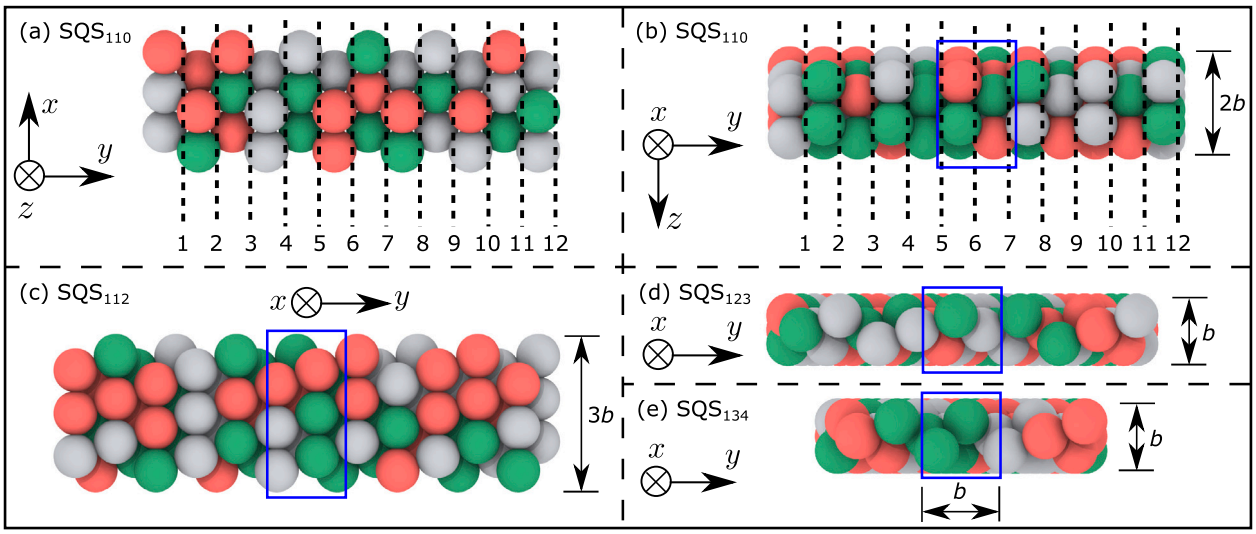

Fig. 1. Atomistic structures of (a,b) SQS_{110}, (c) SQS_{112}, (d) SQS_{123}, and (e) SQS_{134}. Red, green, and gray atoms are, respectively, Mo, Nb, and Ti in MoNbTi MPEA, and Nb, Ti, and Zr in NbTiZr MPEA. The crystallographic orientations are: $x\langle 112\rangle$, $y\langle 110\rangle$, and $z\langle 111\rangle$ in SQS_{110}, $x\langle 110\rangle$, $y\langle 112\rangle$, and $z\langle 111\rangle$ in SQS_{112}, $x\langle 145\rangle$, $y\langle 123\rangle$, and $z\langle 111\rangle$ in SQS_{123}, and $x\langle 257\rangle$, $y\langle 134\rangle$, and $z\langle 111\rangle$ in SQS_{134}. Along the y direction, there are 12 {110}, 24 {112}, 28 {123}, and 26 {134} atomic planes, respectively, in the four SQS. Atoms within the blue boxes in (b–e) are taken into account in plotting the USFE-composition maps in Fig. 6, Fig. 7, and Fig. 8. Visualization was realized via OVITO [50].

$$V_{ij}^{A}(R^{ij}) = \sum_{X,Y}^{N_T} c^X c^Y V_{ij}^{XY}(R^{ij}) \tag{6}$$

$$\langle \tilde{\rho}_i \rangle = \sum_{\substack{j \\ j\neq i}}^{N_{nei}} \sum_{X}^{N_T} c^X \rho_{ij}^{X}(R^{ij}) \tag{7}$$

where N_T is the number of elemental types, and c^X and c^Y are atomic concentrations of elements X and Y, respectively. In addition, the average atomic mass $m^A = \sum_X^{N_T} c^X m^X$ and the average cutoff distance $r_c^A = \sum_X^{N_T} c^X r_c^X$. Hereinafter, to distinguish the two types of potentials, the A-atom potential will be denoted by a subscript "A", while the alloy potential has no subscript.

Among the four MPEA potentials used here, only the NbTiZr and $NbTiZr_A$ potentials have been benchmarked against DFT calculations [39]. Toward validating both potentials for MoNbTi, we calculate some essential quantities, such as the lattice parameter a_0, cohesive energy E_{coh}, and elastic constants $\boldsymbol{C}$, using MS, and in Section 2.5, compare these results to those based on DFT and available experimental data.

2.2. Method: Special quasirandom structures

Constructing the atomic models used in MS and DFT calculations for the MPEAs begins with a 3D representative volume of a random solid solution of the three elements in equal amounts. Special quasi-random structures (SQS) [51] using ATAT [52] are first built and then used as building blocks of larger simulation cells for subsequent calculations. For each ternary MPEA, three SQS are used. Each SQS is defined by its y axis, which lies normal to one of the four types of slip planes: {110}, {112}, {123}, and {134} planes. We denote these four SQS as SQS_{110}, SQS_{112}, SQS_{123}, and SQS_{134}. In all, the z axis is directed along $\langle 111\rangle$, which is the shift direction, and the x-axis lies in-plane in the transverse direction. The magnitude of the Burgers vector of a full dislocation $\mathbf{b} = (a_0/2)\langle 111\rangle$ is the same for all cases. Let L_x, L_y, and L_z, respectively, be the edge lengths of the SQS along the x, y, and z directions. As shown in Fig. 1, SQS_{110} has 72 atoms and 12 {110} atomic planes, with $L_z = 2b$; SQS_{112} has 72 atoms and 24 {112} planes, with $L_z = 3b$; SQS_{123} has 84 atoms and 28 {123} planes, with $L_z = b$; last, SQS_{134} has 78 atoms and 26 {134} planes, with $L_z = b$. In these 3D volumes, the cross-sectional area on the slip plane, $A_{gsf} = L_x L_z$, ranges approximately from 40 to 80 Å^2.

2.3. Method: Molecular statics

MS simulations are carried out using LAMMPS [53]. To calculate the lattice parameter a_0, a series of periodic simulation cells containing SQS_{110} of different sizes are used, and for each size, the energy is calculated. For the cell size with the smallest bulk energy E_{bulk}, a_0 and cohesive energy E_{coh} are obtained. For example, for MoNbTi, we have

$$E_{coh}^{MoNbTi} = \frac{E_{free}^{Mo} + E_{free}^{Nb} + E_{free}^{Ti}}{3} - \frac{E_{bulk}^{MoNbTi}}{N_{bulk}} \tag{8}$$

where N_{bulk} is the number of atoms in the bulk (for SQS_{110}, $N_{bulk} = 72$), and $E_{free} = 0$ is the energy of a free atom in MS simulations. This procedure is repeated for SQS_{112}, SQS_{123}, and SQS_{134}. We find that among the four SQS, both a_0 and E_{coh} differ by less than 1%. Once a_0 is determined, the stiffness tensor $\boldsymbol{C}$ is calculated via the stress–strain approach.

2.4. Method: Density functional theory

DFT calculations are conducted in MoNbTi via VASP [54]. Based on the projector augmented wave method [55,56], a pseudopotential using a plane-wave basis with a cutoff energy of 336.876 eV is adopted. To approximate the exchange–correlation energy functional, the Perdew–Burke–Ernzerhof formulation of the generalized gradient approximation is used [57]. The conjugate gradient scheme is employed for the electronic self-consistent loop. Convergence is reached when the total free energy change between two steps are smaller than 10^{-4} eV [58]. The Brillouin zone is constructed by the Monkhorst–Pack scheme [59], with a smearing width of 0.2 eV based on the Methfessel–Paxton smearing method [60].

In DFT, we use similar procedures to calculate a_0, E_{coh}, and $\boldsymbol{C}$ as those described earlier for MS. For a_0, E_{bulk}, and $\boldsymbol{C}$, the free energy without ionic relaxation is calculated with a k-point mesh of $5 \times 3 \times 8$. Unlike in MS simulations, the energy of a free atom, E_{free}, is usually not zero in DFT and is calculated by considering one atom in a cube of 15 Å × 15 Å × 15 Å with a single k-point, with magnetism taken into account. Note that in all other DFT calculations, magnetism is not considered. The elastic tensor $\boldsymbol{C}$ is calculated in AELAS [61] via the energy-strain approach, which in theory yields the same result as the stress–strain method [62].

Table 1
Lattice parameter a_0 (in Å), cohesive energy E_{coh} (in eV), effective BCC elastic constants $C_{11}^{\dagger}$, $C_{12}^{\dagger}$, and $C_{44}^{\dagger}$ (in GPa), Zener ratio A_c, isotropic Poisson's ratio in Hill form ν^{H}, isotropic shear modulus in Hill form μ^{H} (in GPa), and isotropic Young's modulus in Hill form E_Y^{H} (in GPa), of MoNbTi and NbTiZr predicted by MS simulations. MS_A denote results obtained based on the A-atom potentials for MPEAs. MS results in Mo, Nb, as well as those from current and prior DFT calculations and prior experiments (Exp) are also presented. For E_Y^{H}, all results are based on single crystals, except the two experimental results for MPEAs [36,37] which are based on polycrystals.

Material	Method	a_0	E_{coh}	$C_{11}^{\dagger}$	$C_{12}^{\dagger}$	$C_{44}^{\dagger}$	A_c	ν^{H}	μ^{H}	E_Y^{H}
Mo	MS	3.135	6.81	458.76	167.84	114.32	0.79	0.29	125.9	326.03
	DFT [63]	3.16	6.35	467.85	158.75	100.22	0.65	0.3	119.29	310.67
	Exp [64]	3.147		465	163	109	0.72	0.3	124.22	322.09
	Exp [65]		6.82							
Nb	MS	3.3	7.57	263.56	125.28	35.03	0.51	0.38	46.16	127.07
	DFT [63]	3.324	6.91	249.01	135.43	18.1	0.32	0.42	29.23	83.02
	Exp [64]	3.301		245	132	28.4	0.5	0.4	37.55	104.9
	Exp [65]		7.57							
MoNbTi	MS_A	3.234	6.42	251.85	138.84	78.72	1.39	0.33	68.93	182.97
	MS	3.234	6.42	241.23	134.48	76.8	1.44	0.33	66.38	176.22
	DFT	3.225	6.21	252.13	134.11	32.41	0.55	0.39	41.29	114.78
	DFT [66]	3.227								
	DFT [67]	3.239		290.9	128.1	61.5	0.76	0.33	68.81	183.37
	Exp [36]	3.23								183 ± 30
NbTiZr	MS_A	3.399	6.29	149.57	111.46	61.47	3.23	0.36	38.51	104.73
	MS	3.399	6.29	141.32	111.7	57.63	3.89	0.37	33.61	92.36
	DFT [39]	3.39		143	111	64	4	0.36	36.95	100.69
	Exp [37]	3.4								80.4

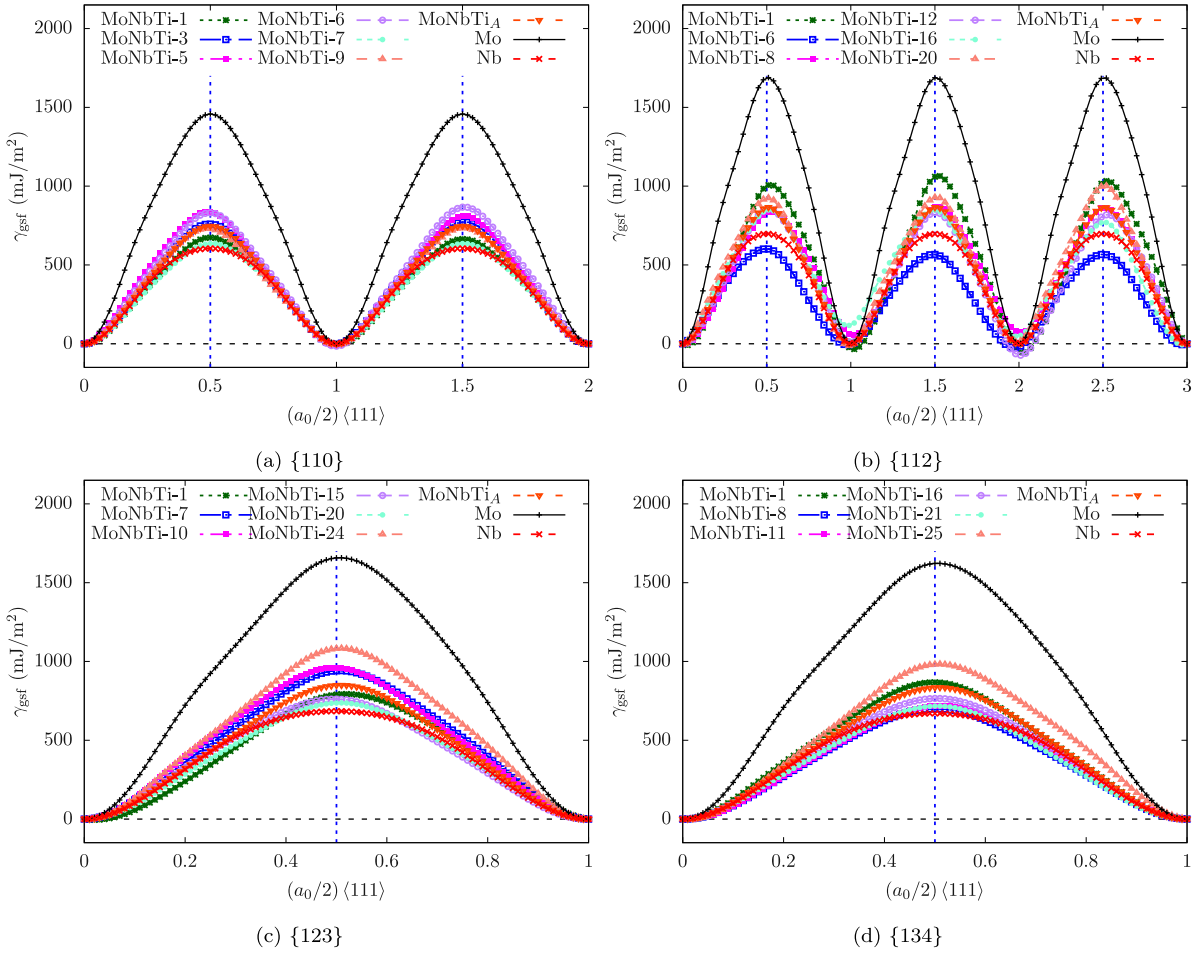

Fig. 2. Selected GSFE curves on four types of slip planes in MoNbTi, based on MS simulations using alloy and A-atom potentials. For each type of slip plane, only selected GSFE curves are presented with the plane indices included in the keys. Corresponding DFT results for three lower order planes are presented in Fig. 4.

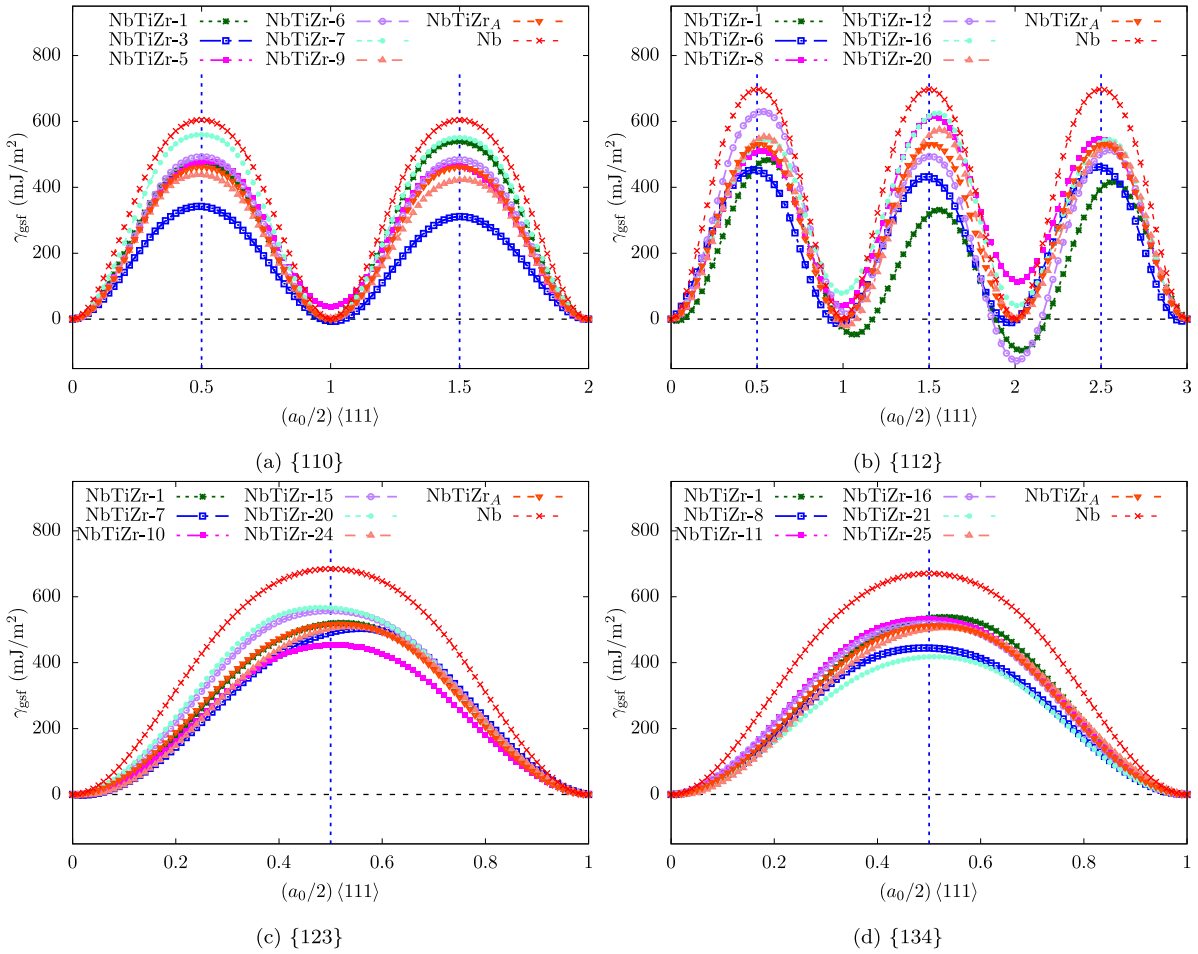

Fig. 3. Selected GSFE curves on four types of slip planes in NbTiZr, based on MS simulations using alloy and *A*-atom potentials. For each type of slip plane, only selected GSFE curves are presented with the plane indices included in the keys.

2.5. A comparison between MS, DFT, and experiments

Table 1 presents the lattice parameters a_0 and cohesive energies E_{coh}, calculated by MS and compares them to current and prior DFT calculations, as well as experiments. As shown, a_0 and E_{coh} are in good agreement among MS, DFT, and the measurements.

Also compared in Table 1 are the elastic constants. For pure metals, including Mo, Nb, and two MPEAs using their *A*-atom potentials, the elastic tensor $\boldsymbol{C}$ has three independent constants, C_{11}, C_{12}, and C_{44}. However, for relatively small super cells of MPEAs, the BCC crystalline symmetry can be broken [34]. Based on MS simulations in the standard x[100], y[010], z[001] framework, $\boldsymbol{C}$ for MoNbTi and NbTiZr using their alloy potentials are, respectively,

$$\begin{bmatrix} 242.68 & & & & & \\ 134.86 & 242.69 & & & & \\ 134.28 & 134.29 & 238.32 & & \text{Symm} & \\ -0.12 & -0.46 & -0.49 & 76.74 & & \\ -0.18 & 0.31 & -0.23 & 0.17 & 76.95 & \\ -0.83 & -0.38 & -0.76 & 0.25 & -0.15 & 76.71 \end{bmatrix}, \tag{9}$$

$$\begin{bmatrix} 140.07 & & & & & \\ 111.66 & 140.07 & & & & \\ 111.9 & 111.55 & 143.82 & & \text{Symm} & \\ -0.15 & 0.06 & 0.16 & 57.59 & & \\ 0.83 & 0.26 & 0.8 & 1.8 & 57.44 & \\ 0.02 & 0.32 & -0.84 & 0.62 & 0.21 & 57.86 \end{bmatrix}. \tag{10}$$

On the other hand, the elastic constants for MoNbTi from DFT calculations are

$$\begin{bmatrix} 253.76 & & & & & \\ 137.91 & 249.2 & & & & \\ 128.61 & 135.82 & 253.42 & & \text{Symm} & \\ -3.9 & 0.2 & 1.38 & 31.22 & & \\ -1.69 & -5.4 & 2.42 & -3.87 & 27.81 & \\ 0.51 & 0.31 & -4.39 & 0.96 & 3.28 & 38.19 \end{bmatrix} \tag{11}$$

where all components are in reasonable agreement with those based on MS (Eq. (9)) except C_{44}, C_{55}, and C_{66}. This is, however, expected because our prior DFT calculations in FCC [68] and BCC [63] pure metals showed that DFT-based values of C_{44} (which equals C_{55} and C_{66} in these metals) are almost always lower than those in experiments.

We then determine the effective BCC elastic constants from the calculated results, using the following relationships [34]

$$C_{11}^{\dagger} = \frac{C_{11} + C_{22} + C_{33}}{3} \tag{12}$$

$$C_{12}^{\dagger} = \frac{C_{12} + C_{13} + C_{23}}{3} \tag{13}$$

$$C_{44}^{\dagger} = \frac{C_{44} + C_{55} + C_{66}}{3} \tag{14}$$

Employing the Zener ratio $A_c = 2C_{44}^{\dagger}/(C_{11}^{\dagger} - C_{12}^{\dagger})$ as a measure of the degree of cubic elastic anisotropy, we find that, based on MS simulations, MoNbTi is nearly isotropic ($A_c = 1.44$), while NbTiZr is highly anisotropic ($A_c = 3.89$).

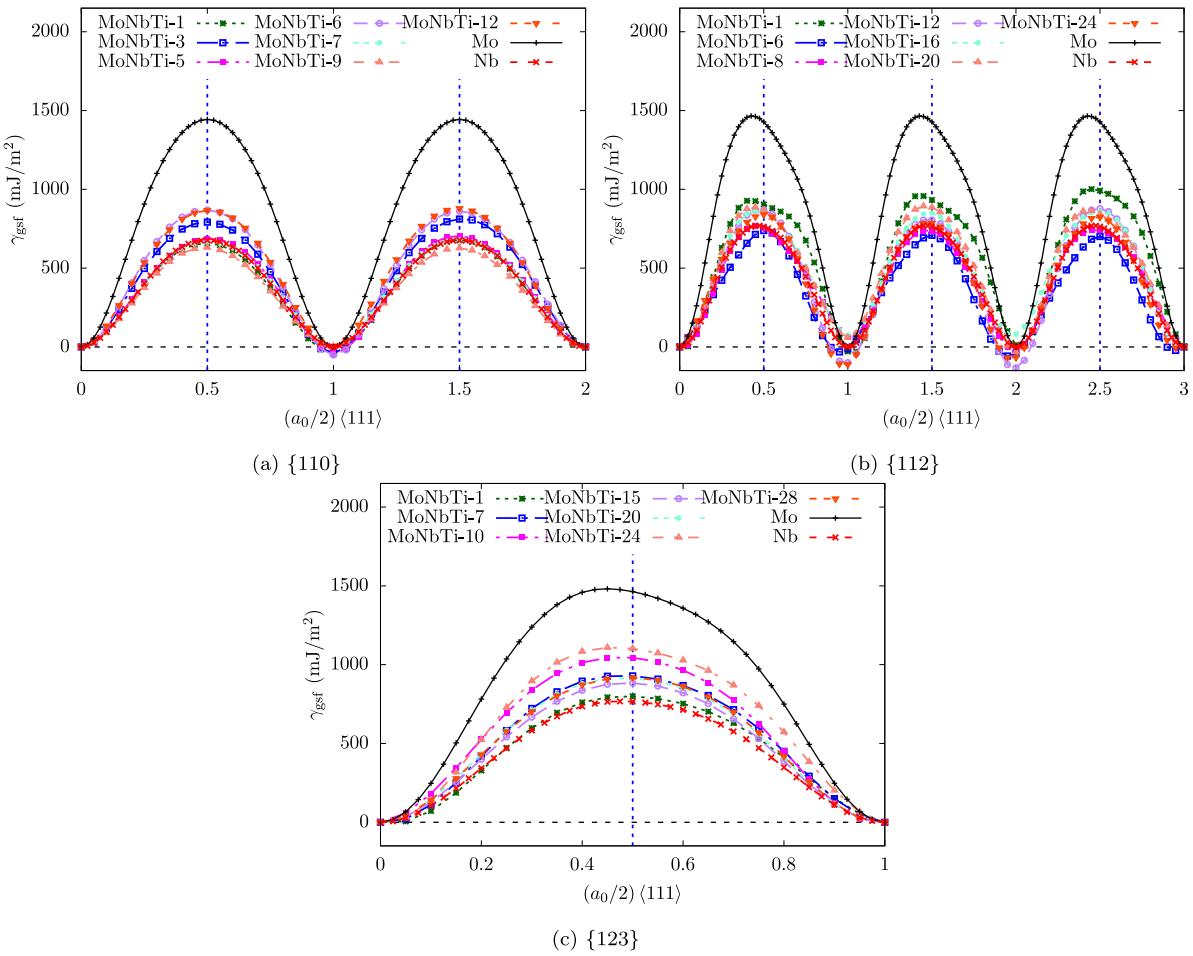

Fig. 4. Selected GSFE curves on three lower order slip planes in MoNbTi, based on DFT calculations. For each type of slip plane, only selected GSFE curves are presented with the plane indices included in the keys.

As another comparison with the experimental data, we need to calculate the Young's modulus from $\boldsymbol{C}$ in order to compare with measurements made on polycrystalline MoNbTi [36] and NbTiZr [37]. To this end, we estimate the equivalent isotropic constants via the Hill average (denoted by the superscript H) [69] because it well reproduces the bulk modulus compared to measurements [18,70]. The isotropic Poisson's ratio ν^{H}, isotropic shear modulus μ^{H}, and isotropic Young's modulus $E_{\mathrm{Y}}^{\mathrm{H}}$ are, respectively,

$$\nu^{\mathrm{H}} = \frac{C_{11}^{\dagger} + 4C_{12}^{\dagger} - 2C_{44}^{\dagger}}{8C_{11}^{\dagger} + 12C_{12}^{\dagger} + 4C_{44}^{\dagger}} + \frac{(C_{11}^{\dagger})^2 + 2C_{12}^{\dagger}(3C_{44}^{\dagger} - C_{12}^{\dagger}) + C_{11}^{\dagger}(C_{12}^{\dagger} - 2C_{44}^{\dagger})}{4[(C_{11}^{\dagger})^2 + C_{12}(C_{44}^{\dagger} - 2C_{12}^{\dagger}) + C_{11}^{\dagger}(C_{12}^{\dagger} + 3C_{44}^{\dagger})]} \tag{15}$$

$$\mu^{\mathrm{H}} = \frac{C_{11}^{\dagger} + 3C_{44}^{\dagger} - C_{12}^{\dagger}}{10} + \frac{5(C_{11}^{\dagger} - C_{12}^{\dagger})C_{44}^{\dagger}}{6C_{11}^{\dagger} - 6C_{12}^{\dagger} + 8C_{44}^{\dagger}} \tag{16}$$

$$E_{\mathrm{Y}}^{\mathrm{H}} = 2\mu^{\mathrm{H}}(1 + \nu^{\mathrm{H}}) \tag{17}$$

Results of ν^{H}, μ^{H}, and $E_{\mathrm{Y}}^{\mathrm{H}}$ are summarized in Table 1. For MoNbTi, our DFT calculations, which use pseudopotentials, predict that $E_{\mathrm{Y}}^{\mathrm{H}}$ = 114.78 GPa. A prior DFT calculation [67], which employed the exact muffin-tin orbitals method, predicted $E_{\mathrm{Y}}^{\mathrm{H}}$ = 183.37 GPa. Using the alloy and *A*-atom potentials, our MS simulations predict $E_{\mathrm{Y}}^{\mathrm{H}}$ = 176.22 GPa and 182.97 GPa, respectively, which are within the range of the experimental value for polycrystals (183 ± 30 GPa) [36].

Based on the reasonable agreement between the values of a_0, E_{coh}, and $\boldsymbol{C}$ from MS simulations and those from available DFT and experimental measurement, we feel confident to use the alloy and *A*-atom potentials for MoNbTi in subsequent GSFE calculations. Later, as a further validation, we will compare some GSFE curves for MoNbTi using DFT with those using MS. As mentioned earlier, we will also calculate GSFEs for NbTiZr using the alloy and *A*-atom potentials in MS. Note that these two potentials have already been benchmarked against DFT [39].

3. Generalized stacking fault energies

3.1. Method: Molecular statics

To calculate the GSFE, γ_{gsf}, a slip plane within the SQS must be selected. Each SQS contains multiple slip planes with distinct atomic arrangements and the value of γ_{gsf} between two distinct slip planes will not be the same [34,35,71,72]. To obtain GSFE curves for each distinct plane in the SQS, the following procedure is used. By way of example, the description focuses on the {110} plane, but the same method is applied to the three higher order planes. SQS_{110} has 12 {110} atomic planes along the *y* direction, from which 12 distinct {110} plane GSFE curves can be calculated. For each realization, denoted as $\mathrm{SQS}_{110}^{\dagger}$, the model is built by sequentially moving the atomic planes in the SQS downwards (from say the top to the bottom), so that each $\mathrm{SQS}_{110}^{\dagger}$ has a different mid-plane (e.g., plane 6 in Fig. 1(a–b)). For each $\mathrm{SQS}_{110}^{\dagger}$, a simulation cell is then constructed by adding a vacuum of 12 Å to its end along the *y* direction such that the periodic images do not interact with each other. It follows then that the top six atomic planes are displaced with respect to the bottom six atomic planes along the $z\langle 111\rangle$ direction. After each displacement, the top two and bottom two

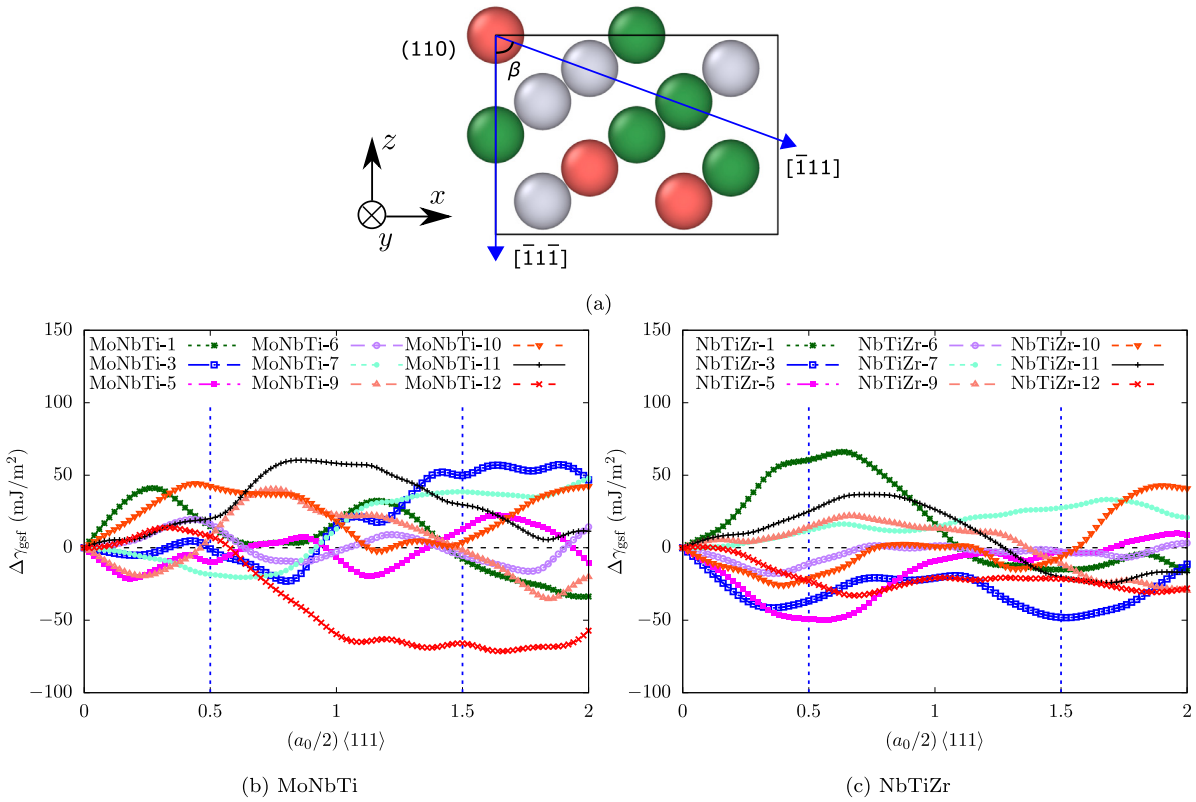

Fig. 5. (a) An illustration of two non-parallel ⟨111⟩ within the same (110) plane, with $\beta = 70.53°$. The atomic structure is taken from SQS_{110}. Shown also are the differences in the GSFE values, $\Delta\gamma_{gsf}$, along the two ⟨111⟩ directions in (b) MoNbTi and (c) NbTiZr. Selected GSFE curves are presented with the plane indices included in the keys. Results are based on MS simulations using alloy potentials.

Table 2
Means ($\bar{\gamma}_{usf}$) and standard deviations (s_{usf}) of USFEs (in mJ/m^2) of MoNbTi and NbTiZr using their alloy potentials on four types of slip planes predicted by MS simulations. MS_{ave} and MS_A, respectively, denote results obtained based on Eq. (21) and the A-atom potentials for MPEAs. Current MS results of Mo and Nb are shown as references. Results from prior DFT calculations for Mo and Nb [63] and current DFT calculations for MoNbTi are also presented.

Plane	Method	Mo	Nb	MoNbTi		NbTiZr	
		γ_{usf}	γ_{usf}	$\bar{\gamma}_{usf}$	s_{usf}	$\bar{\gamma}_{usf}$	s_{usf}
{110}	MS_{ave}			802.01		424.48	
	MS_A			747		461.39	
	MS	1458.05	604.87	744.63	112.38	446.54	66.28
	DFT	1443.39	676.78	764.9	122.76		
{112}	MS_{ave}			925.65		485.69	
	MS_A			866.38		530.98	
	MS	1689.03	697.23	852.1	127.68	503.94	88.09
	DFT	1465.13	768.82	865.3	118.39		
{123}	MS_{ave}			909.57		478.04	
	MS_A			849.89		517.74	
	MS	1657.93	684.71	850.18	129.89	508.76	38
	DFT	1481.35	767.42	910.65	124.83		
{134}	MS_{ave}			891.41		471.07	
	MS_A			835.45		513.05	
	MS	1622.44	670.69	834.75	85.15	503.28	50.97

atomic planes are fixed while the remaining eight planes in the center are allowed to relaxed along the y direction. Energy minimization is realized by combining the conjugate gradient scheme and the fast inertial relaxation engine [73], and is terminated when one of the following two criteria is satisfied: (i) the change in energy between successive iterations divided by the most recent energy magnitude is less than or equal to 10^{-12} and (ii) the length of the global force vector for all atoms is less than or equal to 10^{-12} eV/Å. For each $SQS^{\dagger}_{110}$, the displacement d_z stops when it reaches L_z. In this way, 101 γ_{gsf} values in one GSFE curve are calculated for each $SQS^{\dagger}_{110}$. Following similar procedures, for each MPEA, we further obtain 24 GSFE curves on {112} planes, 28 GSFE curves on {123} planes, and 26 GSFE curves on {134} planes. Note that for the highest order plane, each $SQS^{\dagger}_{134}$, whose L_y is too small, repeats itself once along the y direction before the vacuum is added. The MS calculations are done in both MoNbTi and NbTiZr.

3.2. Method: Density functional theory

In DFT, the same procedure used in MS is followed. A k-point mesh of $5 \times 1 \times 8$ is adopted. The ionic relaxation stops when the total energy between two steps is smaller than 10^{-3} eV/atom. Due to the high computational cost in DFT, 41 values are calculated per GSFE

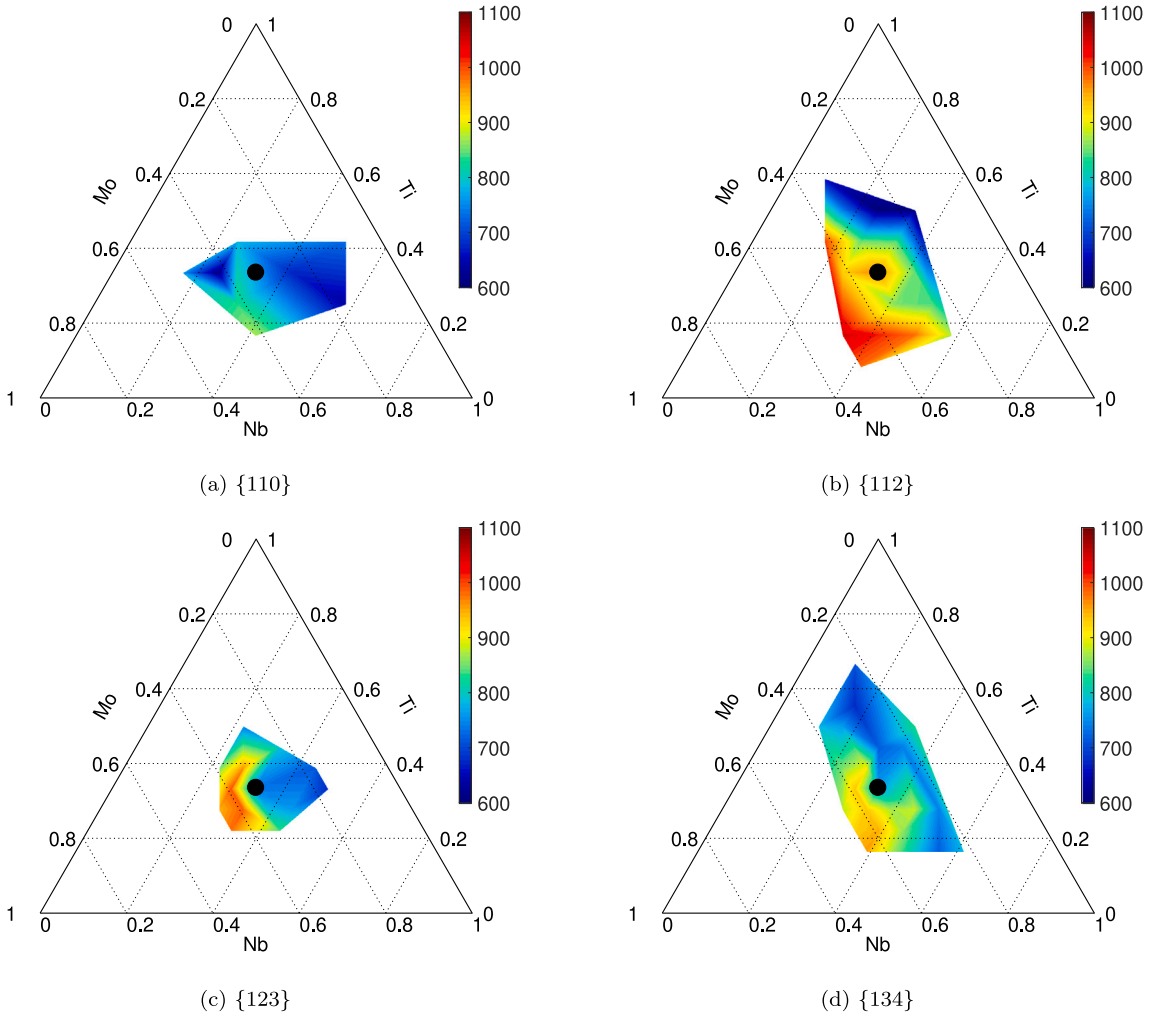

(a) {110} (b) {112}

(c) {123} (d) {134}

Fig. 6. USFE values (in mJ/m^2) correlated with the local chemical compositions on four types of slip planes in MoNbTi. The black circles in the center indicate the equal-molar composition. Results are based on MS using the alloy potential. Corresponding DFT results for three lower order planes are presented in Fig. 8.

curve, and only three lower order planes – {110}, {112}, and {123} – in MoNbTi are considered.

4. Results and discussions

4.1. GSFE curves for the {110} planes

We first examine the {110} GSFE curves calculated via MS for the two MPEAs, presented in Fig. 2(a) and Fig. 3(a). The corresponding GSFE curves in MoNbTi based on DFT are presented in Fig. 4(a). Each {110} GSFE calculation spans displacements over the full edge length L_z, which equals two lattice periodicity distances along the $z\langle 111\rangle$ direction. For reference, the {110} GSFE curves for Mo, Nb, and A-atom potential-based MPEAs are also shown. Both the pure metal and MPEA GSFE curves reach a single peak value within each periodic length b, commonly called the unstable stacking fault energy (USFE), γ_{usf}, and hence, with no local minimum or metastable states. In this respect, the pure metals and MPEAs are similar.

The MPEA GSFE curves, however, exhibit many other properties that deviate from GSFE curves of those of Mo and Nb as well as the effective A-atom pure metal, indicating a significant local MPE effect on the GSFEs. One outstanding MPE effect is the clear variation in properties among the {110} GSFE curves shown for the same MPEA. This dispersion rises from differences in the in-plane chemical composition among the GSFE calculations. Each GSFE curve samples a different crystallographic plane from the 3D random solid solution and the atomic arrangements and compositions in each plane are not the same. The effect is most predominantly seen in the value of γ_{usf}. For similar reasons, variations in local maxima and minima in {111} GSFEs in FCC MPEAs have been reported [71,72]. Table 2 reports the mean and standard deviation in γ_{usf} considering all 24 values for the two MPEAs. It can be expected that in the limit of large sampling planes A_{gsf}, all {110} γ_{usf} would closely match that calculated with the A-atom potential.

Another MPE effect that emerges in these GSFE curves is an in-plane anisotropy between the two distinct $\langle 111\rangle$ directions in each {110} plane. Fig. 5 plots the difference in the variation of GSFE between the two $\langle 111\rangle$ directions belonging to the same specific {110} plane. A pure metal would lead to identical GSFE curves for these two in-plane $\langle 111\rangle$ directions. In contrast, in the MPEAs, we find that the two $\langle 111\rangle$ directions are not equivalent and their GSFE values differ by up to 70 mJ/m^2. The differences emerge not only in the peak value, γ_{usf}, but for all in-plane shear displacements over the entire lattice periodicity distance. Indeed, each atom in MPEAs has neighbors that are of random elemental type, and thus the bond strengths along these two in-plane $\langle 111\rangle$ directions are no longer equivalent as they are in a pure metal. We find here that at least within a short length span, the local chemical variation gives rise to notable in-plane anisotropy with respect to the $\langle 111\rangle$ direction is being sheared as well as sense of direction in which a given direction is sheared.

A final MPEA effect arising from these calculations includes an asymmetry in these GSFE curves, in which the peak value γ_{usf} is not

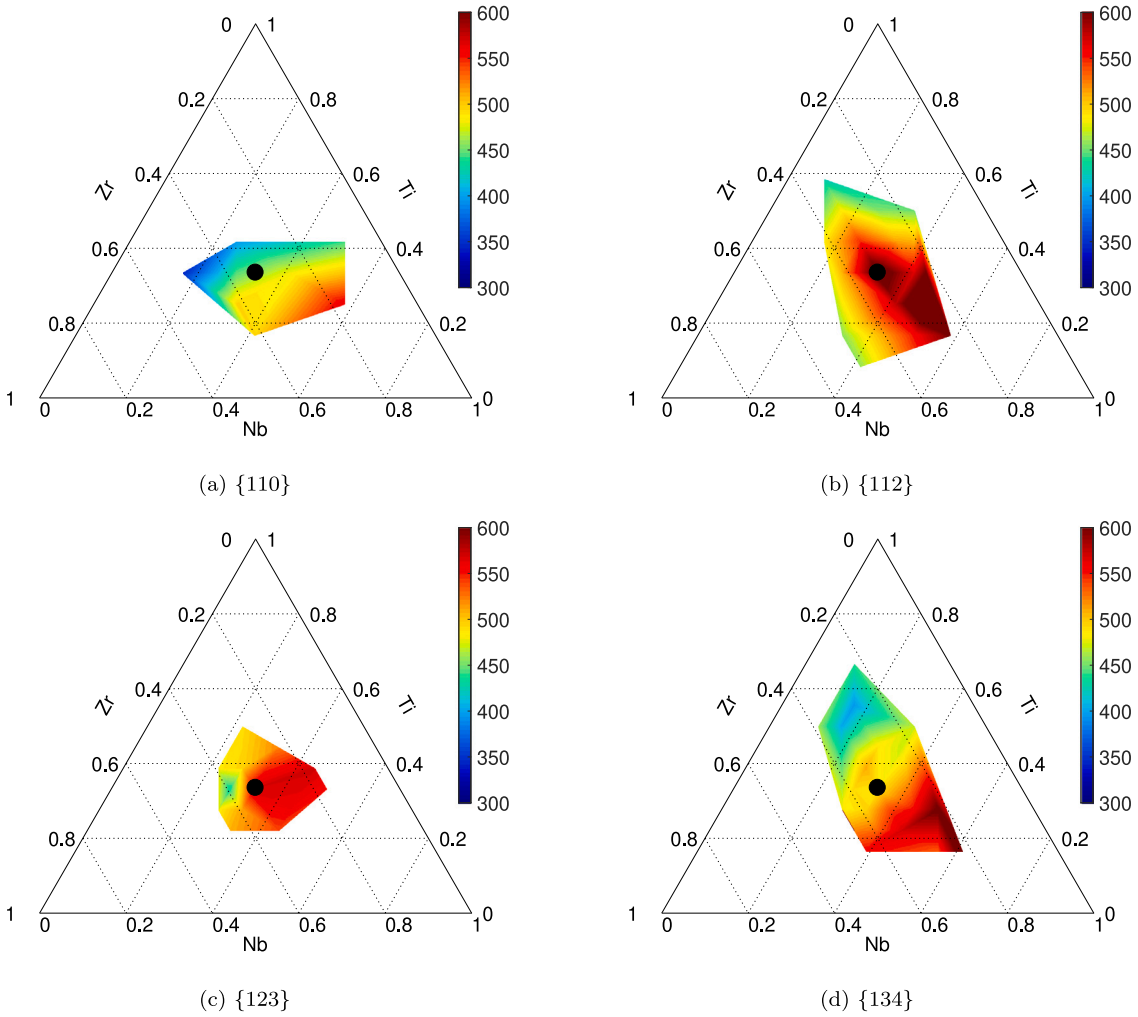

(a) {110} (b) {112}

(c) {123} (d) {134}

Fig. 7. USFE values (in mJ/m^2) correlated with the local chemical compositions on four types of slip planes in NbTiZr. The black circles in the center indicate the equal-molar composition. Results are based on MS using the alloy potential.

achieved at the half lattice shift: $d_z = b/2$ in the first period and $3b/2$ in the second period, as it does in pure metals. This MPEA-induced asymmetry implies that for an MPEA, a single calculation at $b/2$ (or $3b/2$) would not necessarily give the local maximum γ_{usf}, and the variation in the GSFE with $\langle 111 \rangle$ displacement over the full periodic length would need to be calculated to identify γ_{usf}.

These MPEA-induced changes in the fundamental properties of the {110} GSFE could result in large changes in the motion of individual dislocations and noticeable effects on material behavior. The MPEA-induced asymmetry of the {110} GSFE curve would then give rise to an anisotropy in resistance to glide, meaning that the resistance to shear in one direction is not equal to that when shearing in the opposite direction. The variation in the GSFE curves from one periodic region to the next and between the two $\langle 111 \rangle$ directions implies that the slip resistance changes dynamically as the dislocation glides. The variable shear resistance is on the order of the lattice spacing within their habit plane. Further, dislocations gliding on co-planar systems or parallel planes in the same MPEA would experience vastly different resistances.

4.2. GSFE curves for the {112}, {123}, and {134} planes

Next, we examine the GSFE curves calculated for the three higher order planes, {112}, {123}, and {134}, some of which are presented in Fig. 2(b–d) and Fig. 3(b–d), respectively, for MoNbTi and NbTiZr. The corresponding GSFE curves on {112} and {123} planes in MoNbTi based on DFT are presented in Fig. 4(b,c). As mentioned in Section 2.2, the edge lengths of the SQS along the z direction, L_z, are $3b$, b, and b, respectively, for SQS_{112}, SQS_{123}, and SQS_{134}. Therefore, there are three, one, and one period in each {112}, {123}, and {134} GSFE curve, respectively. In each period, we find one peak GSFE value, γ_{usf}, like the {110} plane. Also similarly, one outstanding MPE effect here is the variation in the GSFE curves between even periodic lattice regions in the same specific plane as well as among parallel planes. The shift distance corresponding to γ_{usf} noticeably varies as well. Given the numbers of unique slip planes (24, 28, 26) in each type of SQS, there are 72, 28, and 26 γ_{usf} values, respectively, for these three types of slip planes. Table 2 lists the mean and standard deviation in γ_{usf} on the three higher order planes, which are found to be just as broadly distributed as those on the {110} plane. As before, we find that for the same type of slip plane in the same MPEA, the mean value of γ_{usf} closely matches that obtained from the effective A-atom potential. Again, this suggests that the A-atom potential-based γ_{usf} well represents what would be achieved in the limit of large sampling area.

4.3. Slip plane anisotropy in the USFE

Due to their relation to the resistance to glide by dislocations, local maximum and relative changes in the GSFE curves can provide insight into slip plane selection, particular in BCC crystals where possible slip modes are distinguished by their crystallographic planes [74]. Comparing across the four slip planes {110}, {112}, {123}, and {134} in Mo and Nb, the plane with the lowest γ_{usf} is the {110} plane and the

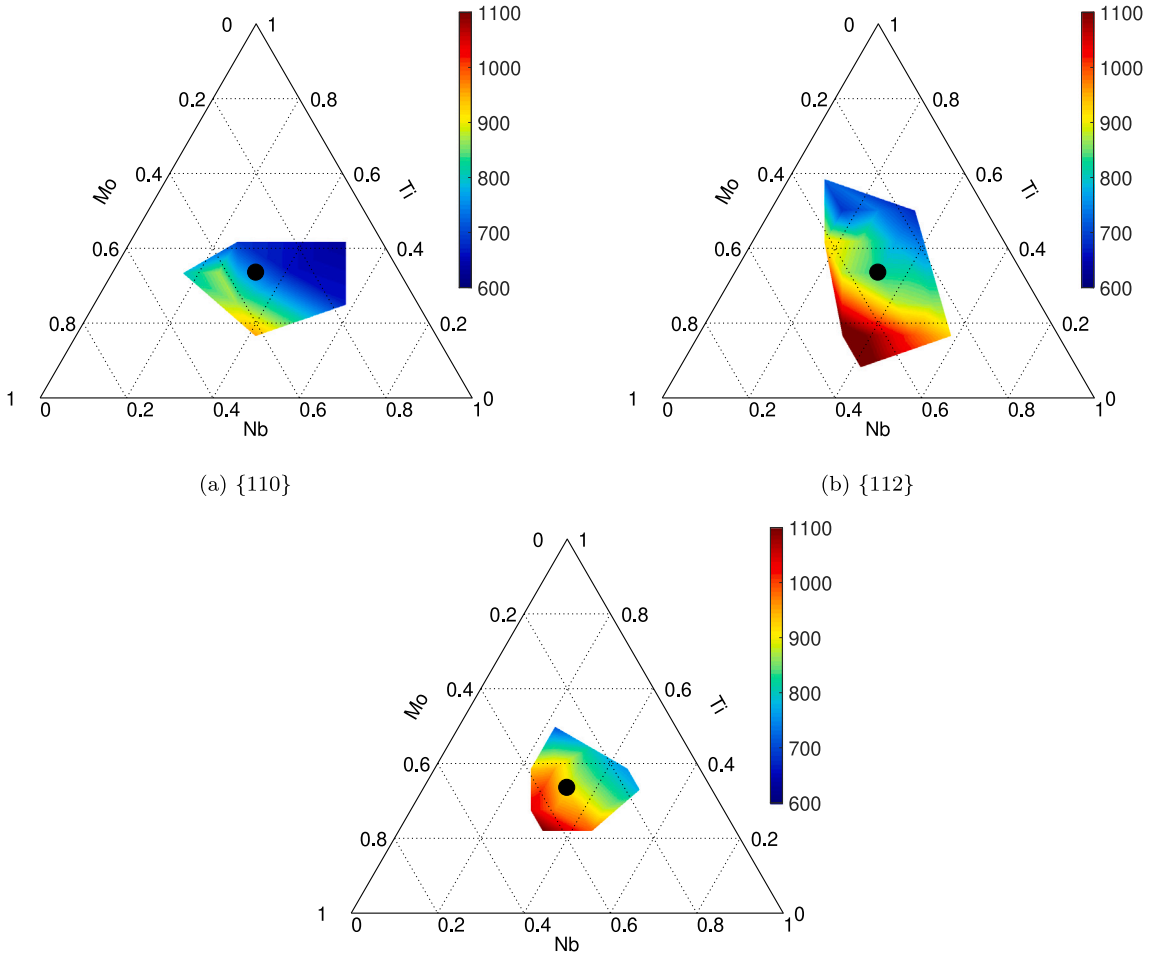

(a) {110} (b) {112}

(c) {123}

Fig. 8. USFE values (in mJ/m^2) correlated with the local chemical compositions on three lower order slip planes in MoNbTi, based on DFT calculations. The black circles in the center indicate the equal-molar composition.

three higher order planes, {112}, {123}, and {134}, have similar γ_{usf}. This order is preserved in MPEAs, for both that based on the *A*-atom potential and the mean value based on the alloy potential. In other words,

$$\gamma_{\text{usf}}^{110} < \gamma_{\text{usf}}^{112} \approx \gamma_{\text{usf}}^{123} \approx \gamma_{\text{usf}}^{134}, \tag{18}$$

$$\bar{\gamma}_{\text{usf}}^{110} < \bar{\gamma}_{\text{usf}}^{112} \approx \bar{\gamma}_{\text{usf}}^{123} \approx \bar{\gamma}_{\text{usf}}^{134}. \tag{19}$$

One noticeable MPE effect here is the reduction in the difference between γ_{usf} between the three higher order planes in MPEAs, compared with the pure metals. Reduced anisotropy in the shear resistance among slip modes, however small, suggests a rise in the number of available slip modes and overall more uniform plastic deformation on all possible slip planes.

Taken together, our results show that, on the same type of slip plane, the mean γ_{usf} value for MoNbTi lies between γ_{usf} for pure Mo and pure Nb, and the mean γ_{usf} value for NbTiZr is below that for Nb. In summary

$$\gamma_{\text{usf}}^{\text{Mo}} > \bar{\gamma}_{\text{usf}}^{\text{MoNbTi}} \approx \gamma_{\text{usf}}^{\text{MoNbTi}_A} > \gamma_{\text{usf}}^{\text{Nb}} > \bar{\gamma}_{\text{usf}}^{\text{NbTiZr}} \approx \gamma_{\text{usf}}^{\text{NbTiZr}_A}. \tag{20}$$

4.4. Non-degenerate energy states

In a pure metal, whether the constituent Mo or Nb, or the *A*-atom potential-based MPEA, the energetic states at every periodic lattice spacing is degenerate. Often, the GSFE of the starting state is set to zero. In-plane shear displacements corresponding to every periodic lattice recovers the atomic arrangement leading to the same energetic state, and therefore, the GSFE is zero again. For an MPEA, however, after a full periodic lattice shift, the type and arrangement of the neighboring atoms across the plane change. Consequently, after one periodic shift the GSFE is not necessarily zero and could either rise or fall, or in other words, the difference, or the residual energy at $d_z = nb$, where integer valued $n = 1, 2, \ldots$, could be either positive or negative.

To quantify the residual energy for the {110} and {112} planes, the simulation cells used in calculation were made such that $L_z > b$, to permit shear displacements to cover two or more consecutive lattice periodicity distances. Recall in Fig. 2(a,b) and Fig. 3(a,b), the calculated {110} GSFE for two periodic spacings and {112} GSFE for three periodic spacings are shown. For the {110} GSFE curves in both MPEAs, the energetic state is not recovered after each shift of b, and the residual energies range from −6.6 mJ/m^2 to 36.85 mJ/m^2 in NbTiZr. For the {112} GSFE curves, the residual energies are even larger, ranging from −126.85 mJ/m^2 to 114.2 mJ/m^2 for NbTiZr. Non-degenerate energy states were also reported in an FCC CoCrNi MPEA [27], indicating that the initial configuration does not have the lowest bulk energy among all possible in-plane shifts. One may, in theory, use the configuration with the lowest energy as the reference, and thereby "elevating" all GSFE values to non-negative. Nevertheless, a different γ_{gsf} value after a rigid shift by b suggests that the bypass of a full dislocation would create a local, anti-phase boundary, which carries energy [75].

Table 3
Lattice parameter a_0 (in Å) and USFEs γ_{usf} (in mJ/m^2) of BCC Ti and BCC Zr on the four types of slip planes predicted by MS simulations.

	a_0	γ_{usf}			
		{110}	{112}	{123}	{134}
BCC Ti	3.3	343.11	390.68	386.08	381.1
BCC Zr	3.597	325.46	369.17	363.33	361.43

4.5. Effect of chemical composition on the USFE

The finite area glide planes taken from the 3D volume of random solid solution deviate in their chemical make up from the 1:1:1 equi-molar ternary compositions. Their chemical differences offer the opportunity to identify relationships between local chemical composition and GSFEs. To quantify the effect, we calculate the composition of the constituent elements among all atoms within a distance of $b/2$ from the slip plane along the y direction, as indicated by the blue boxes in Fig. 1(b–e), which corresponds to 1, 2, 3, and 3 layers of atoms on one side of the {110}, {112}, {123}, and {134} planes, respectively. Fig. 6 and Fig. 7 present the γ_{usf} values mapped onto a ternary diagram for these two MPEAs. In MoNbTi, it is found that a larger fraction of Mo atoms and a smaller fraction of Nb atoms are associated with a higher γ_{usf}. The DFT calculations in MoNbTi, presented in Fig. 8, show similar trends. These results are expected because Mo has a higher γ_{usf} than Nb. In NbTiZr, a larger fraction of Nb atoms and a smaller fraction of Ti atoms result in a higher γ_{usf} value. This, however, is not as easy to predict because Ti has HCP lattices in ambient conditions.

To further explore this problem, we calculate the GSFEs in BCC Ti and BCC Zr, which may form in alloys or under high pressures [76,77]. First, the lattice parameter a_0 for Ti and Zr in their equilibrium BCC phase are calculated. Then the GSFE curves on the {110}, {112}, {123}, and {134} planes are calculated. Table 3 shows that the values of γ_{usf} in BCC Ti and BCC Zr on all planes are much lower than those of Mo and Nb. These explain the composition-γ_{usf} correlation discovered earlier in NbTiZr.

With these data and ignoring the effect of local interactions between neighboring atoms, one could crudely estimate γ_{usf} for the MPEAs as the number weighted after average of the γ_{usf} for the three constituent metals in their BCC phases. For example, for MoNbTi, the rule-of-mixtures approximation for γ_{usf} for any given plane is given by

$$\gamma_{usf}^{ave} = \frac{\gamma_{usf}^{Mo} + \gamma_{usf}^{Nb} + \gamma_{usf}^{Ti}}{3} \tag{21}$$

Results of γ_{usf}^{ave} in both MPEAs are presented in Table 2. Although there may be no physical justification to take a volume-weighted average of the constituent γ_{usf}, thereby ignoring the atomic-scale elemental interactions, we find that the volume average in Eq. (21) provides a reasonable estimate. It helps us understand Eq. (20) qualitatively. For example, $\bar{\gamma}_{usf}$ for NbTiZr lies below that of Nb due to the low γ_{usf} values in BCC Ti and BCC Zr. In addition, this rough estimate can be useful when precise values for γ_{usf} are not needed, such as in sifting through various compositions and for identifying potential slip modes. It is also far easier to find reliable interatomic potentials for pure metals than alloys.

5. Conclusions

In this work, we conduct MS simulations to calculate the GSFE curves in two refractory MPEAs with BCC structures: MoNbTi and NbTiZr. Four types of slip planes – {110}, {112}, {123}, and {134} – are considered. The main findings are summarized as follows:

(1) With a finite nanometer cross-sectional area on the slip plane, the local chemical composition in the slip plane and its immediate vicinity deviates from the nominal solid solution. The consequence is a wide range of GSFE values among parallel slip planes for the same MPEA.
(2) The alloy potential and a newly developed A-atom potential for MoNbTi are validated by comparing the MS-based lattice parameter, cohesive energy, and elastic constants against those from DFT and available experimental data, the latter of which include lattice parameter and Young's modulus. Interested readers can find and download the A-atom potentials for both MPEAs at https://github.com/wrj2018/Intermetallics_2020.
(3) On the {110} planes, unlike the case of pure metals, the MPEA GSFE curves are asymmetric and the two GSFE curves along two coplanar, non-parallel ⟨111⟩ directions are not the same.
(4) In each MPEA, for the same type of slip plane, the mean USFE value based on the alloy potential is close to that based on the A-atom potential.
(5) Due to the atom-to-atom elemental variation in the MPEA, shear displacements of one lattice periodicity length may transition the system to a higher or lower energetic state, rather than recovering the original reference state. The residual energies are more pronounced in NbZrTi than in MoNbTi.
(6) Among the two MPEAs and two BCC pure metals (Mo and Nb), the mean USFE is the highest in Mo, the second highest in MoNbTi, followed by Nb, and finally, the lowest in NbTiZr (Eq. (20)).
(7) By directly correlating USFE with the local chemical compositions in Fig. 5, we find that a larger fraction of Mo atoms or a smaller fraction of Nb atoms in MoNbTi leads to a higher USFE. A larger fraction of Nb atoms or a smaller fraction of Ti atoms in NbTiZr increases the USFE value.

CRediT authorship contribution statement

Shuozhi Xu: Conceptualization, Methodology, Formal analysis, Investigation, Data curation, Writing - original draft, Writing - review & editing, Visualization. **Emily Hwang:** Investigation, Software. **Wu-Rong Jian:** Software, Validation, Writing - review & editing. **Yanqing Su:** Investigation, Software, Formal analysis, Writing - review & editing. **Irene J. Beyerlein:** Conceptualization, Resources, Writing - review & editing, Supervision, Funding acquisition.

Declaration of competing interest

The authors declare that they have no known competing financial interests or personal relationships that could have appeared to influence the work reported in this paper.

Acknowledgments

We thank Dr. Satish Rao for providing the alloy potential files for MPEAs, and Dr. Wolfram G. Nöhring and Dr. Xiangguo Li for helpful discussions. The work of SX was supported in part by the Elings Prize Fellowship in Science offered by the California NanoSystems Institute (CNSI) on the UC Santa Barbara campus. SX, YS, and IJB gratefully acknowledge support from the Office of Naval Research under contract ONR BRC Grant N00014-18-1-2392. EH acknowledges the Future Leaders in Advanced Materials (FLAM) program sponsored by the Materials Research Laboratory at UC Santa Barbara. The work of WJ was in part supported by the Regents in Mechanical Engineering Fellowship awarded by UC Santa Barbara. Use was made of computational facilities purchased with funds from the National Science Foundation (CNS-1725797) and administered by the Center for Scientific Computing (CSC). The CSC is supported by the CNSI and the Materials Research Science and Engineering Center (MRSEC; NSF DMR 1720256) at UC Santa Barbara. This work used the Extreme Science and Engineering Discovery Environment (XSEDE), which is supported by National Science Foundation grant number ACI-1053575.

References

[1] H.Y. Diao, R. Feng, K.A. Dahmen, P.K. Liaw, Fundamental deformation behavior in high-entropy alloys: An overview, Concentrated Solid Solution Alloys Perspective, Curr. Opin. Solid State Mater. Sci. 21 (5) (2017) 252–266, http://dx.doi.org/10.1016/j.cossms.2017.08.003, URL http://www.sciencedirect.com/science/article/pii/S135902861730147X.

[2] Y.F. Ye, Q. Wang, J. Lu, C.T. Liu, Y. Yang, High-entropy alloy: challenges and prospects, Mater. Today 19 (6) (2016) 349–362, http://dx.doi.org/10.1016/j.mattod.2015.11.026, URL http://www.sciencedirect.com/science/article/pii/S1369702115004010.

[3] J.-W. Yeh, S.-K. Chen, S.-J. Lin, J.-Y. Gan, T.-S. Chin, T.-T. Shun, C.-H. Tsau, S.-Y. Chang, Nanostructured high-entropy alloys with multiple principal elements: novel alloy design concepts and outcomes, Adv. Eng. Mater. 6 (5) (2004) 299–303, http://dx.doi.org/10.1002/adem.200300567, URL https://onlinelibrary.wiley.com/doi/abs/10.1002/adem.200300567.

[4] B. Cantor, I.T.H. Chang, P. Knight, A.J.B. Vincent, Microstructural development in equiatomic multicomponent alloys, Mater. Sci. Eng. A 375–377 (2004) 213–218, http://dx.doi.org/10.1016/j.msea.2003.10.257, URL http://www.sciencedirect.com/science/article/pii/S0921509303009936.

[5] Z. Li, S. Zhao, R.O. Ritchie, M.A. Meyers, Mechanical properties of high-entropy alloys with emphasis on face-centered cubic alloys, Prog. Mater. Sci. 102 (2019) 296–345, http://dx.doi.org/10.1016/j.pmatsci.2018.12.003, URL http://www.sciencedirect.com/science/article/pii/S0079642518301178.

[6] O.N. Senkov, G.B. Wilks, D.B. Miracle, C.P. Chuang, P.K. Liaw, Refractory high-entropy alloys, Intermetallics 18 (9) (2010) 1758–1765, http://dx.doi.org/10.1016/j.intermet.2010.05.014, URL http://www.sciencedirect.com/science/article/pii/S0966979510002475.

[7] J.P. Couzinié, G. Dirras, Body-centered cubic high-entropy alloys: From processing to underlying deformation mechanisms, Mater. Charact. 147 (2019) 533–544, http://dx.doi.org/10.1016/j.matchar.2018.07.015, URL http://www.sciencedirect.com/science/article/pii/S1044580318307514.

[8] O.N. Senkov, S. Gorsse, D.B. Miracle, High temperature strength of refractory complex concentrated alloys, Acta Mater. 175 (2019) 394–405, http://dx.doi.org/10.1016/j.actamat.2019.06.032, URL http://www.sciencedirect.com/science/article/pii/S1359645419304033.

[9] O.N. Senkov, D.B. Miracle, K.J. Chaput, J.-P. Couzinié, Development and exploration of refractory high entropy alloys —a review, J. Mater. Res. 33 (19) (2018) 3092–3128, http://dx.doi.org/10.1557/jmr.2018.153, URL https://www.cambridge.org/core/journals/journal-of-materials-research/article/development-and-exploration-of-refractory-high-entropy-alloysa-review/2268206F3D4B2F18DD86FD5A0662E06D.

[10] E.P. George, D. Raabe, R.O. Ritchie, High-entropy alloys, Nat. Rev. Mater. 4 (8) (2019) 515–534, http://dx.doi.org/10.1038/s41578-019-0121-4, URL https://www.nature.com/articles/s41578-019-0121-4.

[11] P.M. Anderson, J.P. Hirth, J. Lothe, Theory of Dislocations, third ed., Cambridge University Press, Cambridge, 2017.

[12] V. Vítek, R.C. Perrin, D.K. Bowen, The core structure of $\frac{1}{2}\langle 111\rangle$ screw dislocations in b.c.c. crystals, Phil. Mag. A 21 (173) (1970) 1049–1073, http://dx.doi.org/10.1080/14786437008238490.

[13] P. Tu, Y. Zheng, C. Zhuang, X. Zeng, H. Zhu, A high-throughput computation framework for generalized stacking fault energies of pure metals, Comput. Mater. Sci. 159 (2019) 357–364, http://dx.doi.org/10.1016/j.commatsci.2018.12.013, URL http://www.sciencedirect.com/science/article/pii/S0927025618307924.

[14] V. Vitek, Structure of dislocation cores in metallic materials and its impact on their plastic behaviour, Prog. Mater. Sci. 36 (1992) 1–27, http://dx.doi.org/10.1016/0079-6425(92)90003-P, URL http://www.sciencedirect.com/science/article/pii/007964259290003P.

[15] S. Xu, J.R. Mianroodi, A. Hunter, I.J. Beyerlein, B. Svendsen, Phase-field-based calculations of the disregistry fields of static extended dislocations in FCC metals, Phil. Mag. 99 (11) (2019) 1400–1428, http://dx.doi.org/10.1080/14786435.2019.1582850.

[16] S. Xu, L. Smith, J.R. Mianroodi, A. Hunter, B. Svendsen, I.J. Beyerlein, A comparison of different continuum approaches in modeling mixed-type dislocations in Al, Modelling Simul. Mater. Sci. Eng. 27 (7) (2019) 074004, 10.1088/1361-651X/ab2d16.

[17] D. Hull, D.J. Bacon, Introduction to Dislocations, fifth ed., Butterworth-Heinemann, 2011.

[18] S. Xu, Y. Su, I.J. Beyerlein, Modeling dislocations with arbitrary character angle in face-centered cubic transition metals using the phase-field dislocation dynamics method with full anisotropic elasticity, Mech. Mater. 139 (2019) 103200, http://dx.doi.org/10.1016/j.mechmat.2019.103200, URL http://www.sciencedirect.com/science/article/pii/S0167663619303734.

[19] S.M. Hafez Haghighat, J. von Pezold, C.P. Race, F. Körmann, M. Friák, J. Neugebauer, D. Raabe, Influence of the dislocation core on the glide of the $\frac{1}{2}\langle 111\rangle 110$ edge dislocation in bcc-iron: An embedded atom method study, Comput. Mater. Sci. 87 (2014) 274–282, http://dx.doi.org/10.1016/j.commatsci.2014.02.031, URL http://www.sciencedirect.com/science/article/pii/S0927025614001256.

[20] A. Hunter, I.J. Beyerlein, Relationship between monolayer stacking faults and twins in nanocrystals, Acta Mater. 88 (2015) 207–217, http://dx.doi.org/10.1016/j.actamat.2014.12.045, URL http://www.sciencedirect.com/science/article/pii/S1359645414009719.

[21] A. Kumar, M.A. Kumar, I.J. Beyerlein, First-principles study of crystallographic slip modes in ω-Zr, Sci. Rep. 7 (1) (2017) 1–9, http://dx.doi.org/10.1038/s41598-017-09153-w, URL https://www.nature.com/articles/s41598-017-09153-w.

[22] M. Ardeljan, M. Knezevic, M. Jain, S. Pathak, A. Kumar, N. Li, N.A. Mara, J.K. Baldwin, I.J. Beyerlein, Room temperature deformation mechanisms of Mg/Nb nanolayered composites, J. Mater. Res. 33 (10) (2018) 1311–1332, http://dx.doi.org/10.1557/jmr.2018.107, URL https://www.cambridge.org/core/journals/journal-of-materials-research/article/room-temperature-deformation-mechanisms-of-mgnb-nanolayered-composites/FDF2B0509E3D83DE478261AF5BE26A22.

[23] P. Andric, B. Yin, W.A. Curtin, Stress-dependence of generalized stacking fault energies, J. Mech. Phys. Solids 122 (2019) 262–279, http://dx.doi.org/10.1016/j.jmps.2018.09.007, URL http://www.sciencedirect.com/science/article/pii/S0022509618305751.

[24] S.L. Shang, W.Y. Wang, B.C. Zhou, Y. Wang, K.A. Darling, L.J. Kecskes, S.N. Mathaudhu, Z.K. Liu, Generalized stacking fault energy, ideal strength and twinnability of dilute Mg-based alloys: A first-principles study of shear deformation, Acta Mater. 67 (2014) 168–180, http://dx.doi.org/10.1016/j.actamat.2013.12.019, URL http://www.sciencedirect.com/science/article/pii/S1359645413009543.

[25] D. Buey, L.G. Hector, M. Ghazisaeidi, Core structure and solute strengthening of second-order pyramidal $\langle c+a\rangle$ dislocations in mg-y alloys, Acta Mater. 147 (2018) 1–9, http://dx.doi.org/10.1016/j.actamat.2017.12.066, URL http://www.sciencedirect.com/science/article/pii/S1359645418300223.

[26] Y.Q. Guo, S.H. Zhang, I.J. Beyerlein, D. Legut, S.L. Shang, Z.K. Liu, R.F. Zhang, Synergetic effects of solute and strain in biocompatible Zn-based and Mg-based alloys, Acta Mater. 181 (2019) 423–438, http://dx.doi.org/10.1016/j.actamat.2019.09.059, URL http://www.sciencedirect.com/science/article/pii/S1359645419306524.

[27] Q.-J. Li, H. Sheng, E. Ma, Strengthening in multi-principal element alloys with local-chemical-order roughened dislocation pathways, Nature Comm. 10 (1) (2019) 1–11, http://dx.doi.org/10.1038/s41467-019-11464-7, URL https://www.nature.com/articles/s41467-019-11464-7.

[28] R. Gröger, V. Vitek, A. Dlouhý, Effective pair potential for random fcc CoCrFeMnNi alloys, Modelling Simul. Mater. Sci. Eng. (2020) http://dx.doi.org/10.1088/1361-651X/ab7f8b, URL http://iopscience.iop.org/10.1088/1361-651X/ab7f8b.

[29] W. Li, S.I. Rao, Q. Wang, H. Fan, J. Yang, J.A. El-Awady, Core structure and mobility of edge dislocations in face-centered-cubic chemically complex NiCoFe and NiCoFeCu equiatomic solid-solution alloys, Materialia 9 (2020) 100628, http://dx.doi.org/10.1016/j.mtla.2020.100628, URL http://www.sciencedirect.com/science/article/pii/S2589152920300454.

[30] S.I. Rao, C. Woodward, T.A. Parthasarathy, O. Senkov, Atomistic simulations of dislocation behavior in a model FCC multicomponent concentrated solid solution alloy, Acta Mater. 134 (2017) 188–194, http://dx.doi.org/10.1016/j.actamat.2017.05.071, URL http://www.sciencedirect.com/science/article/pii/S1359645417304603.

[31] E. Antillon, C. Woodward, S.I. Rao, B. Akdim, T.A. Parthasarathy, Chemical short range order strengthening in a model FCC high entropy alloy, Acta Mater. 190 (2020) 29–42, http://dx.doi.org/10.1016/j.actamat.2020.02.041, URL http://www.sciencedirect.com/science/article/pii/S1359645420301543.

[32] R. Pasianot, D. Farkas, Atomistic modeling of dislocations in a random quinary high-entropy alloy, Comput. Mater. Sci. 173 (2020) 109366, http://dx.doi.org/10.1016/j.commatsci.2019.109366, URL http://www.sciencedirect.com/science/article/pii/S0927025619306652.

[33] S. Zhao, G.M. Stocks, Y. Zhang, Stacking fault energies of face-centered cubic concentrated solid solution alloys, Acta Mater. 134 (2017) 334–345, http://dx.doi.org/10.1016/j.actamat.2017.05.001, URL http://www.sciencedirect.com/science/article/pii/S1359645417303671.

[34] Y. Su, S. Xu, I.J. Beyerlein, *Ab initio*-informed phase-field modeling of dislocation core structures in equal-molar CoNiRu multi-principal element alloys, Modelling Simul. Mater. Sci. Eng. 27 (8) (2019) 084001, http://dx.doi.org/10.1088/1361-651X/ab3b62.

[35] S. Zhao, Y. Osetsky, G.M. Stocks, Y. Zhang, Local-environment dependence of stacking fault energies in concentrated solid-solution alloys, npj Comput. Mater. 5 (1) (2019) 13, http://dx.doi.org/10.1038/s41524-019-0150-y, URL https://www.nature.com/articles/s41524-019-0150-y.

[36] O.N. Senkov, S.I. Rao, T.M. Butler, K.J. Chaput, Ductile Nb alloys with reduced density and cost, J. Alloys Compd. 808 (2019) 151685, http://dx.doi.org/10.1016/j.jallcom.2019.151685, URL http://www.sciencedirect.com/science/article/pii/S0925838819329184.

[37] O.N. Senkov, S. Rao, K.J. Chaput, C. Woodward, Compositional effect on microstructure and properties of NbTiZr-based complex concentrated alloys, Acta Mater. 151 (2018) 201–215, http://dx.doi.org/10.1016/j.actamat.2018.03.065, URL http://www.sciencedirect.com/science/article/pii/S1359645418302635.

[38] O.N. Senkov, C. Zhang, A.L. Pilchak, E.J. Payton, C. Woodward, F. Zhang, CALPHAD-aided development of quaternary multi-principal element refractory alloys based on NbTiZr, J. Alloys Compd. 783 (2019) 729–742, http://dx.doi.org/10.1016/j.jallcom.2018.12.325, URL http://www.sciencedirect.com/science/article/pii/S0925838818348837.

[39] S.I. Rao, B. Akdim, E. Antillon, C. Woodward, T.A. Parthasarathy, O.N. Senkov, Modeling solution hardening in BCC refractory complex concentrated alloys: NbTiZr, $Nb_{1.5}TiZr_{0.5}$ and $Nb_{0.5}TiZr_{1.5}$, Acta Mater. 168 (2019) 222–236, http://dx.doi.org/10.1016/j.actamat.2019.02.013, URL http://www.sciencedirect.com/science/article/pii/S1359645419300916.

[40] M.S. Daw, M.I. Baskes, Embedded-atom method: Derivation and application to impurities, surfaces, and other defects in metals, Phys. Rev. B 29 (12) (1984) 6443–6453, http://dx.doi.org/10.1103/PhysRevB.29.6443, URL http://link.aps.org/doi/10.1103/PhysRevB.29.6443.

[41] X.W. Zhou, R.A. Johnson, H.N.G. Wadley, Misfit-energy-increasing dislocations in vapor-deposited CoFe/NiFe multilayers, Phys. Rev. B 69 (14) (2004) 144113, http://dx.doi.org/10.1103/PhysRevB.69.144113, URL http://link.aps.org/doi/10.1103/PhysRevB.69.144113.

[42] D.-Y. Lin, S.S. Wang, D.L. Peng, M. Li, X.D. Hui, An *n*-body potential for a Zr-Nb system based on the embedded-atom method, J. Phys.: Condens. Matter 25 (10) (2013) 105404, http://dx.doi.org/10.1088/0953-8984/25/10/105404.

[43] F. Maresca, W.A. Curtin, Theory of screw dislocation strengthening in random BCC alloys from dilute to "High-Entropy" alloys, Acta Mater. 182 (2020) 144–162, http://dx.doi.org/10.1016/j.actamat.2019.10.007, URL http://www.sciencedirect.com/science/article/pii/S1359645419306676.

[44] F. Maresca, W.A. Curtin, Mechanistic origin of high strength in refractory BCC high entropy alloys up to 1900K, Acta Mater. 182 (2020) 235–249, http://dx.doi.org/10.1016/j.actamat.2019.10.015, URL http://www.sciencedirect.com/science/article/pii/S1359645419306755.

[45] M.R. Fellinger, H. Park, J.W. Wilkins, Force-matched embedded-atom method potential for niobium, Phys. Rev. B 81 (14) (2010) 144119, http://dx.doi.org/10.1103/PhysRevB.81.144119, URL https://link.aps.org/doi/10.1103/PhysRevB.81.144119.

[46] H. Park, M.R. Fellinger, T.J. Lenosky, W.W. Tipton, D.R. Trinkle, S.P. Rudin, C. Woodward, J.W. Wilkins, R.G. Hennig, *Ab initio* based empirical potential used to study the mechanical properties of molybdenum, Phys. Rev. B 85 (2012) 214121, http://dx.doi.org/10.1103/PhysRevB.85.214121, URL https://journals.aps.org/prb/abstract/10.1103/PhysRevB.85.214121.

[47] C. Varvenne, A. Luque, W.G. Nöhring, W.A. Curtin, Average-atom interatomic potential for random alloys, Phys. Rev. B 93 (10) (2016) 104201, http://dx.doi.org/10.1103/PhysRevB.93.104201, URL https://link.aps.org/doi/10.1103/PhysRevB.93.104201.

[48] W.G. Nöhring, W.A. Curtin, Thermodynamic properties of average-atom interatomic potentials for alloys, Modelling Simul. Mater. Sci. Eng. 24 (4) (2016) 045017, http://dx.doi.org/10.1088/0965-0393/24/4/045017.

[49] S.I. Rao, C. Varvenne, C. Woodward, T.A. Parthasarathy, D. Miracle, O.N. Senkov, W.A. Curtin, Atomistic simulations of dislocations in a model BCC multicomponent concentrated solid solution alloy, Acta Mater. 125 (2017) 311–320, http://dx.doi.org/10.1016/j.actamat.2016.12.011, URL http://www.sciencedirect.com/science/article/pii/S1359645416309478.

[50] A. Stukowski, Visualization and analysis of atomistic simulation data with OVITO—the Open Visualization Tool, Modelling Simul. Mater. Sci. Eng. 18 (1) (2010) 015012, http://dx.doi.org/10.1088/0965-0393/18/1/015012, URL http://iopscience.iop.org/0965-0393/18/1/015012.

[51] A. Zunger, S.-H. Wei, L.G. Ferreira, J.E. Bernard, Special quasirandom structures, Phys. Rev. Lett. 65 (3) (1990) 353–356, http://dx.doi.org/10.1103/PhysRevLett.65.353, URL https://link.aps.org/doi/10.1103/PhysRevLett.65.353.

[52] A. van de Walle, P. Tiwary, M. de Jong, D.L. Olmsted, M. Asta, A. Dick, D. Shin, Y. Wang, L.Q. Chen, Z.K. Liu, Efficient stochastic generation of special quasirandom structures, CALPHAD 42 (2013) 13–18, http://dx.doi.org/10.1016/j.calphad.2013.06.006, URL http://www.sciencedirect.com/science/article/pii/S0364591613000540.

[53] S. Plimpton, Fast parallel algorithms for short-range molecular dynamics, J. Comput. Phys. 117 (1) (1995) 1–19, http://dx.doi.org/10.1006/jcph.1995.1039, URL http://www.sciencedirect.com/science/article/pii/S002199918571039X.

[54] G. Kresse, J. Furthmüller, Efficient iterative schemes for *ab initio* total-energy calculations using a plane-wave basis set, Phys. Rev. B 54 (16) (1996) 11169–11186, http://dx.doi.org/10.1103/PhysRevB.54.11169, URL http://link.aps.org/doi/10.1103/PhysRevB.54.11169.

[55] P.E. Blöchl, Projector augmented-wave method, Phys. Rev. B 50 (24) (1994) 17953–17979, http://dx.doi.org/10.1103/PhysRevB.50.17953, URL http://link.aps.org/doi/10.1103/PhysRevB.50.17953.

[56] G. Kresse, D. Joubert, From ultrasoft pseudopotentials to the projector augmented-wave method, Phys. Rev. B 59 (3) (1999) 1758–1775, http://dx.doi.org/10.1103/PhysRevB.59.1758, URL http://link.aps.org/doi/10.1103/PhysRevB.59.1758.

[57] J.P. Perdew, K. Burke, M. Ernzerhof, Generalized gradient approximation made simple, Phys. Rev. Lett. 77 (18) (1996) 3865–3868, http://dx.doi.org/10.1103/PhysRevLett.77.3865, URL http://link.aps.org/doi/10.1103/PhysRevLett.77.3865.

[58] Y. Su, M. Ardeljan, M. Knezevic, M. Jain, S. Pathak, I.J. Beyerlein, Elastic constants of pure body-centered cubic Mg in nanolaminates, Comput. Mater. Sci. 174 (2020) 109501, http://dx.doi.org/10.1016/j.commatsci.2019.109501, URL http://www.sciencedirect.com/science/article/pii/S0927025619308006.

[59] H.J. Monkhorst, J.D. Pack, Special points for Brillouin-zone integrations, Phys. Rev. B 13 (12) (1976) 5188–5192, http://dx.doi.org/10.1103/PhysRevB.13.5188, URL https://link.aps.org/doi/10.1103/PhysRevB.13.5188.

[60] M. Methfessel, A.T. Paxton, High-precision sampling for brillouin-zone integration in metals, Phys. Rev. B 40 (6) (1989) 3616–3621, http://dx.doi.org/10.1103/PhysRevB.40.3616, URL http://link.aps.org/doi/10.1103/PhysRevB.40.3616.

[61] S.H. Zhang, R.F. Zhang, AELAS: Automatic ELAStic property derivations via high-throughput first-principles computation, Comput. Phys. Comm. 220 (2017) 403–416, http://dx.doi.org/10.1016/j.cpc.2017.07.020, URL http://www.sciencedirect.com/science/article/pii/S0010465517302400.

[62] M.A. Caro, S. Schulz, E.P. O'Reilly, Comparison of stress and total energy methods for calculation of elastic properties of semiconductors, J. Phys.: Condens. Matter 25 (2) (2012) 025803, http://dx.doi.org/10.1088/0953-8984/25/2/025803.

[63] S. Xu, Y. Su, L.W. Smith, I. Beyerlein, Frank-Read source operation in six body-centered cubic refractory metals, J. Mech. Phys. Solids 141 (2020) 104017, http://dx.doi.org/10.1016/j.jmps.2020.104017, URL http://www.sciencedirect.com/science/article/pii/S0022509620302520.

[64] H. Warlimont, W. Martienssen (Eds.), Springer Handbook of Materials Data, second ed., in: Springer Handbooks, Springer International Publishing, 2018, URL https://www.springer.com/us/book/9783319697413.

[65] C. Kittel, Introduction to Solid State Physics, eighth ed., Wiley, Hoboken, NJ, 2004.

[66] S. Huang, E. Holmström, O. Eriksson, L. Vitos, Mapping the magnetic transition temperatures for medium- and high-entropy alloys, Intermetallics 95 (2018) 80–84, http://dx.doi.org/10.1016/j.intermet.2018.01.016, URL http://www.sciencedirect.com/science/article/pii/S0966979517311688.

[67] H. Ge, F. Tian, Y. Wang, Elastic and thermal properties of refractory high-entropy alloys from first-principles calculations, Comput. Mater. Sci. 128 (2017) 185–190, http://dx.doi.org/10.1016/j.commatsci.2016.11.035, URL http://www.sciencedirect.com/science/article/pii/S0927025616305961.

[68] Y. Su, S. Xu, I.J. Beyerlein, Density functional theory calculations of generalized stacking fault energy surfaces for eight face-centered cubic transition metals, J. Appl. Phys. 126 (10) (2019) 105112, http://dx.doi.org/10.1063/1.5115282, URL https://aip.scitation.org/doi/10.1063/1.5115282.

[69] R. Hill, The elastic behaviour of a crystalline aggregate, Proc. R. Soc. Lond. Ser. A Math. Phys. Eng. Sci. 65 (5) (1952) 349–354, http://dx.doi.org/10.1088/0370-1298/65/5/307.

[70] S. Xu, J.R. Mianroodi, A. Hunter, B. Svendsen, I.J. Beyerlein, Comparative modeling of the disregistry and Peierls stress for dissociated edge and screw dislocations in Al, Int. J. Plast. 129 (2020) 102689, http://dx.doi.org/10.1016/j.ijplas.2020.102689, URL http://www.sciencedirect.com/science/article/pii/S0749641919303808.

[71] M. Beyramali Kivy, M. Asle Zaeem, Generalized stacking fault energies, ductilities, and twinnabilities of CoCrFeNi-based face-centered cubic high entropy alloys, Scr. Mater. 139 (2017) 83–86, http://dx.doi.org/10.1016/j.scriptamat.2017.06.014, URL http://www.sciencedirect.com/science/article/pii/S1359646217303172.

[72] J. Ding, Q. Yu, M. Asta, R.O. Ritchie, Tunable stacking fault energies by tailoring local chemical order in CrCoNi medium-entropy alloys, Proc. Natl. Acad. Sci. USA 115 (36) (2018) 8919–8924, http://dx.doi.org/10.1073/pnas.1808660115, URL https://www.pnas.org/content/115/36/8919.

[73] E. Bitzek, P. Koskinen, F. Gähler, M. Moseler, P. Gumbsch, Structural relaxation made simple, Phys. Rev. Lett. 97 (17) (2006) 170201, http://dx.doi.org/10.1103/PhysRevLett.97.170201, URL http://link.aps.org/doi/10.1103/PhysRevLett.97.170201.

[74] C.R. Weinberger, B.L. Boyce, C.C. Battaile, Slip planes in bcc transition metals, Int. Mater. Rev. 58 (5) (2013) 296–314, http://dx.doi.org/10.1179/1743280412Y.0000000015, URL http://www.maneyonline.com/doi/abs/10.1179/1743280412Y.0000000015.

[75] E. Ma, Unusual dislocation behavior in high-entropy alloys, Scr. Mater. 181 (2020) 127–133, http://dx.doi.org/10.1016/j.scriptamat.2020.02.021, URL http://www.sciencedirect.com/science/article/pii/S135964622030097X.

[76] R. Ahuja, L. Dubrovinsky, N. Dubrovinskaia, J.M.O. Guillen, M. Mattesini, B. Johansson, T. Le Bihan, Titanium metal at high pressure: Synchrotron experiments and *ab initio* calculations, Phys. Rev. B 69 (18) (2004) 184102, http://dx.doi.org/10.1103/PhysRevB.69.184102, URL https://link.aps.org/doi/10.1103/PhysRevB.69.184102.

[77] J.S. Pigott, N. Velisavljevic, E.K. Moss, D. Popov, C. Park, J.A.V. Orman, N. Draganic, Y.K. Vohra, B.T. Sturtevant, Room-temperature compression and equation of state of body-centered cubic zirconium, J. Phys.: Condens. Matter 32 (12) (2019) 12LT02, http://dx.doi.org/10.1088/1361-648X/ab5e6e.